Signal Processing 138 (2017) 273–279

Contents lists available at ScienceDirect

Signal Processing

journal homepage: www.elsevier.com/locate/sigpro

A novel unitary PARAFAC method for DOD and DOA estimation in bistatic MIMO radar

Baoqing Xu[a], Yongbo Zhao[a,b,*], Zengfei Cheng[a], Hui Li[a]

[a] National Lab of Radar Signal Processing, Xidian University, Xi'an, 710071, People's Republic of China
[b] Collaborative Innovation Center of Information Sensing and Understanding, Xidian University, Xi'an, 710071, People's Republic of China

ARTICLE INFO

Article history:
Received 21 December 2016
Revised 14 March 2017
Accepted 15 March 2017
Available online 18 March 2017

Keywords:
Multiple-input multiple-output radar
Angle estimation
Real-valued tensor
Parallel factor decomposition

ABSTRACT

In this paper, a novel unitary parallel factor (U-PARAFAC) algorithm of estimating direction-of-departure (DOD) and direction-of-arrival (DOA) in bistatic multiple-input multiple-output (MIMO) radar is proposed. A real-valued tensor signal model is constructed by applying the traditional forward-backward averaging technique. Subsequently, the fact that the real-valued tensor follows a PARAFAC model is proved, thus the subspace-based high-order singular value decomposition (HOSVD) method can be avoided in the subsequent solving process. Furthermore, directly operating the real-valued loading factors instead of the signal subspace, traditional unitary ESPRIT (U-ESPRIT) method is firstly extended to the real-valued PARAFAC model. The new algorithm, which exploits the multidimensional structure and does not require the estimation of signal subspace, having good performance especially at low signal-to-noise ratio (SNR). More attractively, compared with classical tensor methods such as the PARAFAC algorithm and the unitary tensor-ESPRIT algorithm, the U-PARAFAC algorithm still performs well without sacrificing array aperture when targets are highly correlated or closely spaced. Additional angle pair-matching is not required. Simulation results verify the effectiveness of the proposed algorithm.

1. Introduction

Since the concept of multiple-input multiple-output (MIMO) was introduced from communication into radar area, it has attracted considerable attention [1,2]. A MIMO radar system transmits orthogonal waveforms and enables the joint processing of the data received by multiple receive antennas. According to the array configuration, MIMO radar can be classified into two types: statistical MIMO radar [3] and colocated MIMO radar [4]. With the transmit and receive antennas widely spaced, the statistical MIMO radar achieves the spatial diversity gain, while in the colocated MIMO radar more degrees of freedom (DOFs) are obtained because of the closely spaced antennas. Colocated MIMO radar includes bistatic MIMO radar and monostatic MIMO radar. In this paper, we investigate angle estimation problem in bistatic MIMO radar.

In bistatic MIMO radar, some algorithms about estimating direction-of-departure (DOD) and direction-of-arrival (DOA) have been proposed recently [5–8]. In [5], DOD and DOA can be estimated by a Capon-based estimator which actually requires two-dimensional (2-D) search, thus suffering from the great computational burden. In [6], the ESPRIT algorithm is applied to estimate angle information without spatial searching, whereas additional angle pair-matching is needed. With lower computational complexity, another subspace-based approach called the propagator method (PM) is introduced in [7], which does not require the singular value decomposition (SVD) of the received data or eigenvalue decomposition (EVD) of the covariance matrix. Unfortunately, the performance of the PM is inferior than that of the ESPRIT algorithm especially at low signal-to-noise ratio (SNR). Ref. [8] presents the unitary ESPRIT (U-ESPRIT) algorithm which provides better estimation accuracy with reduced computational complexity. Due to the influence of forward-backward averaging [9], the U-ESPRIT algorithm can separate two completely coherent sources and offers improved estimation accuracy for correlated signals.

However, all the methods mentioned above reshape the received data into a special structured matrix, which really do not exploit the strong algebraic structure of the received data and cause some losses in performance. A general tool to store and manipulate multidimensional data is known as tensors, which can take full advantage of the multidimensional information. Therefore, it is meaningful to construct a signal model with tensor structure. The core of tensor-based signal processing is the application of the tensor decomposition [10]. Known methods can be broadly classified into two categories: parallel factor (PARAFAC) decomposition and higher-order singular value decomposition (HOSVD). The

* Corresponding author.
E-mail address: ybzhao@xidian.edu.cn (Y. Zhao).

http://dx.doi.org/10.1016/j.sigpro.2017.03.016
0165-1684/

PARAFAC algorithm decomposes a given tensor into a sum of rank-one tensors, while the HOSVD intends to find a set of unitary matrices across different dimensions that simplify the original tensor.

Based on this background, some tensor approaches have been introduced in [11–13]. In [11], the technique of PARAFAC decomposition is directly applied to solve the complex-valued tensor model. Fully exploiting the multidimensional structure of the tensor model, the algorithm has better performance. A popular method to compute the PARAFAC decomposition is the alternating least squares (ALS) algorithm [10], of which the solving process is iterative and involves matrix inversion. Therefore, the computational burden is huge and the convergence rate slows down when the complex-valued tensor model is taken. In [12], a multi-SVD method is proposed, which provides more accurate estimation of signal subspace compared with traditional subspace-based methods. However, the algorithm performs not so well for highly correlated targets. In [13], the unitary tensor-ESPRIT algorithm exploiting the technique of real-valued HOSVD is proposed. This algorithm provides improved estimation accuracy and partial decorrelation ability like the U-ESPRIT algorithm mentioned above. Maximum of two coherent targets are allowed due to the application of forward-backward averaging, and the performance degrades when the condition is not fulfilled. To solve this problem, spatial smoothing [14] is generalized to tensors, leading to the decorrelation of correlated targets. Regretfully, this advantage is obtained by sacrificing the array aperture. The key idea is to split the array into smaller subarrays and to average the covariance matrix over all these subarrays. That is to say, a part of DOFs is consumed for a decorrelation of targets. Moreover, the superiority of the multi-SVD method and the unitary tensor-ESPRIT algorithm is obtained only in the case that the number of targets is less than the number of sensors in at least one of the transmit array and receive array. In fact, it has been proved in [13] that the HOSVD-based unitary tensor-ESPRIT algorithm yields the same result as the matrix approach when the condition mentioned above is not satisfied.

In this paper, we propose a novel unitary PARAFAC (U-PARAFAC) algorithm to improve the angle estimation performance in bistatic MIMO radar, which does not require to estimate the signal subspace and doubles the numbers of received data. Firstly, a real-valued tensor signal model is obtained by using the forward-backward averaging technique. Here, we emphasize that although the unitary tensor-ESPRIT algorithm in [13] also adopts the forward-backward averaging technique, the subsequent processing is based on the HOSVD method. Different from Haardt et al. [13], one contribution of this paper is that we prove the real-valued tensor signal model still satisfies the condition of PARAFAC decomposition, and then the performance can be improved by solving the real-valued PARAFAC model. Secondly, traditional U-ESPRIT method is firstly extended to real-valued PARAFAC model, which directly operates the real-valued loading factors instead of the real-valued signal subspace. The angle information of the same target can be extracted from the corresponding real-valued loading factors without additional angle pair-matching if and only if the uniqueness of PARAFAC is guaranteed. For uncorrelated signals, the U-PARAFAC algorithm has lightly better estimation accuracy than other methods at low SNR. In correlated and closely spaced signals scenarios, the performance of the U-PARAFAC algorithm is shown to be further improved. Simulation results validate the effectiveness of the proposed algorithm.

Notation 1. Scalars are denoted as italic lowercase letters ($a, b, \cdots$), column vectors as boldface lowercase letters ($\boldsymbol{a}$, $\boldsymbol{b}$, $\cdots$), matrices as boldface capital letters ($\boldsymbol{A}$, $\boldsymbol{B}$, $\cdots$). Calligraphic letters ($\mathcal{A}$, $\mathcal{B}$, $\cdots$) are used to denote tensors. Symbols $(\cdot)^{\mathrm{T}}$, $(\cdot)^*$, $(\cdot)^{-1}$, $(\cdot)^{\mathrm{H}}$ and $(\cdot)^{\dagger}$ denote transpose, conjugate, inverse, conjugate transpose and pseudo-inverse operations, respectively. $\otimes$ and $\odot$ denote the Kronecker product operation and Khatri-Rao product (or column-wise Kronecker product) operation. The notation $\mathrm{diag}(\cdot)$ denotes the diagonalization operation. $\mathrm{Re}\{\cdot\}$ and $\mathrm{Im}\{\cdot\}$ denote the real and imaginary part, respectively. The kth column of $\boldsymbol{A}$ is denoted by $\boldsymbol{A}(:, k)$. $\boldsymbol{I}_N$ denotes the $N \times N$ identity matrix. $\|\cdot\|_F$ represents the Frobenius norm.

2. Tensor-based signal model and prerequisites

First, we introduce some prerequisites mainly about tensors, which are presented in [10,15].

Definition 1. (Rank-one Tensor).
The third-order tensor $\mathcal{X} \in \mathbb{C}^{I\times J\times K}$ is rank-one if it can be written as

$$\mathcal{X} = \boldsymbol{a} \circ \boldsymbol{b} \circ \boldsymbol{c} \tag{1}$$

where $\boldsymbol{a} \in \mathbb{C}^{I\times 1}$, $\boldsymbol{b} \in \mathbb{C}^{J\times 1}$ and $\boldsymbol{c} \in \mathbb{C}^{K\times 1}$. Symbol $\circ$ denotes the vector outer product which means $(\boldsymbol{a} \circ \boldsymbol{b} \circ \boldsymbol{c})_{ijk} = a_i b_j c_k$ for all values of indices i, j and k.

Definition 2. (PARAFAC decomposition).
The PARAFAC decomposition of a third-order tensor $\mathcal{X} \in \mathbb{C}^{I\times J\times K}$ is a linear combination of minimum number of rank-one tensors

$$\mathcal{X}_{ijk} = \sum_{r=1}^{R} a_{ir} b_{jr} c_{kr} \Leftrightarrow \mathcal{X} = \sum_{r=1}^{R} \boldsymbol{a}_r \circ \boldsymbol{b}_r \circ \boldsymbol{c}_r \tag{2}$$

where $\boldsymbol{a}_r, \boldsymbol{b}_r, \boldsymbol{c}_r$ are the rth columns of the so-called loading matrices $\boldsymbol{A} \in \mathbb{C}^{I\times R}$, $\boldsymbol{B} \in \mathbb{C}^{J\times R}$, $\boldsymbol{C} \in \mathbb{C}^{K\times R}$, respectively. $\mathcal{X}_{ijk}$ is the (i, j, k)th element of tensor $\mathcal{X}$ while a_{ir}, b_{jr}, c_{kr} respectively represents the (i, r)th, (j, r)th and (k, r)th element of matrices $\boldsymbol{A}$, $\boldsymbol{B}$ and $\boldsymbol{C}$.

Definition 3. (Essential uniqueness of PARAFAC).
The PARAFAC decomposition of a third-order tensor $\mathcal{X}$ is said to be essentially unique if any matrix triplet $(\widetilde{\boldsymbol{A}}, \widetilde{\boldsymbol{B}}, \widetilde{\boldsymbol{C}})$ that fits the model is related to $(\boldsymbol{A}, \boldsymbol{B}, \boldsymbol{C})$ via $\boldsymbol{A} = \widetilde{\boldsymbol{A}}\boldsymbol{\Gamma}\boldsymbol{\Lambda}_1$, $\boldsymbol{B} = \widetilde{\boldsymbol{B}}\boldsymbol{\Gamma}\boldsymbol{\Lambda}_2$, $\boldsymbol{C} = \widetilde{\boldsymbol{C}}\boldsymbol{\Gamma}\boldsymbol{\Lambda}_3$, with $\boldsymbol{\Lambda}_1$, $\boldsymbol{\Lambda}_2$, $\boldsymbol{\Lambda}_3$ arbitrary nonsingular diagonal matrices satisfying $\boldsymbol{\Lambda}_1\boldsymbol{\Lambda}_2\boldsymbol{\Lambda}_3 = \boldsymbol{I}_K$ and $\boldsymbol{\Gamma}$ an arbitrary permutation matrix.

Definition 4. (Mode-n tensor-matrix product).
The mode-n product of $\mathcal{X} \in \mathbb{C}^{I_1\times I_2\times\cdots\times I_N}$ with a matrix $\boldsymbol{A} \in \mathbb{C}^{J_n\times I_n}$ is denoted by $\mathcal{Y} = \mathcal{X}\times_n\boldsymbol{A}$, where $\mathcal{Y} \in \mathbb{C}^{I_1\times I_2\times\cdots\times I_{n-1}\times J_n\times I_{n+1}\times\cdots\times I_N}$ and $\mathcal{Y}_{i_1,i_2,\cdots,i_{n-1},j_n,\cdots,i_N} = \sum_{i_n=1}^{I_n} x_{i_1,i_2,\cdots,i_{n-1},i_n,\cdots,i_N} a_{j_n,i_n}$. Moreover, the mode product satisfies the following properties [10]

$$\mathcal{X}\times_m\boldsymbol{A}\times_n\boldsymbol{B} = \mathcal{X}\times_n\boldsymbol{B}\times_m\boldsymbol{A} \quad (m \neq n) \tag{3}$$

$$\mathcal{X}\times_n\boldsymbol{A}\times_n\boldsymbol{B} = \mathcal{X}\times_n(\boldsymbol{B}\boldsymbol{A}) \tag{4}$$

After the long but necessary preparations above, we start to construct the tensor signal model for bistatic MIMO radar. Consider a bistatic MIMO radar with M transmit antennas and N receive antennas, both of which are half-wavelength spacing uniform linear arrays (ULAs). The M transmit antennas are used to transmit M orthogonal waveforms $\boldsymbol{S} = [\boldsymbol{s}_1, \boldsymbol{s}_2 \cdots, \boldsymbol{s}_M]^{\mathrm{T}} \in \mathbb{C}^{M\times L}$, where L is the number of samples per pulse period. Assuming that there are K targets existing in the far-field, then the output of the receive array in the qth pulse can be written as

$$\boldsymbol{X}_q = \boldsymbol{B}\boldsymbol{\Sigma}_q\boldsymbol{A}^{\mathrm{T}}\boldsymbol{S} + \boldsymbol{W}_q\,,\ q = 1,\ 2, \ldots,\ Q \tag{5}$$

where $\boldsymbol{A} = [\boldsymbol{a}_1, \boldsymbol{a}_2, \cdots, \boldsymbol{a}_K]$ and $\boldsymbol{B} = [\boldsymbol{b}_1, \boldsymbol{b}_2, \cdots, \boldsymbol{b}_K]$ are the $M \times K$ transmit steering matrix and the $N \times K$ receive steering matrix, respectively. Q is the number of pulses during a coherent processing interval (CPI). To simplify the analysis below, we employ the

center of the ULA as the phase reference like [16] and the array manifold becomes conjugate centrosymmetric. Then, the transmit steering vector and the receive steering vector can be written as

$$\boldsymbol{a}_k = \left[e^{-j\pi\left(\frac{M-1}{2}\right)\sin\theta_k}, \ldots, 1, \ldots, e^{j\pi\left(\frac{M-1}{2}\right)\sin\theta_k}\right]^{\mathrm{T}} \tag{6}$$

$$\boldsymbol{b}_k = \left[e^{-j\pi\left(\frac{N-1}{2}\right)\sin\varphi_k}, \ldots, 1 \cdots, e^{j\pi\left(\frac{N-1}{2}\right)\sin\varphi_k}\right]^{\mathrm{T}} \tag{7}$$

where θ_k and φ_k denote the DOD and DOA of the kth target, respectively. The form of $\boldsymbol{\Sigma}_q$ is given as $\boldsymbol{\Sigma}_q = \mathrm{diag}(\boldsymbol{c}_q)$ with $\boldsymbol{c}_q = [\beta_{1,q}e^{j2\pi f_{d,1}qT_r}, \beta_{2,q}e^{j2\pi f_{d,2}qT_r}, \ldots, \beta_{K,q}e^{j2\pi f_{d,K}qT_r}]^{\mathrm{T}}$, where $\beta_{k,q}$ and $f_{d,k}$ are the RCS coefficient and Doppler frequency of the kth target, respectively. T_r is the pulse repetition time. $\boldsymbol{W}_q \in \mathbb{C}^{N\times L}$ is the additive white Gaussian noise matrix with zero-mean for the qth pulse period and independent of the source signals.

Admittedly, the working environment of radar is very complicated, which makes it difficult to analyse the problem. Therefore, when constructing the signal model of bistatic MIMO radar, we only take the effect of noise into consideration for simplicity. Exploiting the orthogonality property of transmit waveforms which means $(1/L)\boldsymbol{S}\boldsymbol{S}^{\mathrm{H}} = \boldsymbol{I}_M$, (5) is right multiplied by $(1/L)\boldsymbol{S}^{\mathrm{H}}$. Then, the output of matched filters can be written as

$$\boldsymbol{Y}_q = \boldsymbol{B}\boldsymbol{\Sigma}_q\boldsymbol{A}^{\mathrm{T}} + \overline{\boldsymbol{W}}q, \ q = 1, 2, \ldots, Q \tag{8}$$

where $\overline{\boldsymbol{W}}_q = (1/L)\boldsymbol{W}_q\boldsymbol{S}^{\mathrm{H}} \in \mathbb{C}^{N\times M}$ is the noise matrix after matched filters. Then, we stack the matrices $\boldsymbol{Y}_q$, $q = 1, 2, \ldots, Q$, along the third dimension to construct the $N \times M \times Q$ measurement tensor $\mathcal{X}$. In [11], this tensor-based signal model is given by

$$\mathcal{X} = \sum_{k=1}^{K} \boldsymbol{b}_k \circ \boldsymbol{a}_k \circ \boldsymbol{d}_k + \mathcal{N} \tag{9}$$

where $\boldsymbol{C} = [\boldsymbol{c}_1, \boldsymbol{c}_2, \ldots, \boldsymbol{c}_Q]^{\mathrm{T}} = [\boldsymbol{d}_1, \boldsymbol{d}_2, \ldots, \boldsymbol{d}_K]$. K is the number of targets. $\boldsymbol{d}_k$ denotes the kth column of matrix $\boldsymbol{C}$. $\mathcal{N} \in \mathbb{C}^{N\times M\times Q}$ represents the noise term contained in the received data. Ignoring the effects of noises, $\mathcal{X}$ is constructed by K rank-one tensors and thus following the PARAFAC model in line with Definition 2. According to Huang et al. [17] and Nion and Sidiropoulos [18], we rewrite (9) as

$$\mathcal{X} = \mathcal{I}_K \times_1 \boldsymbol{B} \times_2 \boldsymbol{A} \times_3 \boldsymbol{c} + \mathcal{N} \tag{10}$$

where $\mathcal{I}_K$ is the $K \times K \times K$ identity tensor. The formula (10) is proved in Appendix A.

3. Unitary PARAFAC algorithm

Instead of solving the complex tensor model directly, some measures are taken to preprocess the model. Here, we emphasis again that although the new proposed algorithm also adopts the same operation like [13,19] to transform the complex tenor model into a real-valued one, there exists essential differences in subsequent processing. Both methods in [13,19] are based on the HOSVD technique, while the new method exploits the real-valued PARAFAC model, despite that we must prove that the real-valued tensor model follows a PARAFAC model first. The performance improvement of the new algorithm is also mainly obtained by solving the real-valued PARAFAC model, which does not require to estimate the signal subspace and also combines the technique of forward-backward averaging.

3.1. Real-valued PARAFAC model

The main contribution of this part is not the method that transforms the complex tensor model into a real-valued one, but to prove this real-valued tensor follows a PARAFAC model. Then we can decompose the real-valued tensor model by the PARAFAC method instead of the subspace-based HOSVD [13,19], thus guaranteeing a performance improvement. To obtain a real-valued tensor signal model, the techniques of forward-backward averaging and unitary transformation are extended to tensor case [13,19].

To simplify the analysis below, we define a new tensor $\overline{\mathcal{X}}$ as

$$\overline{\mathcal{X}} = \mathcal{X}^* \times_1 \boldsymbol{\Pi}_N \times_2 \boldsymbol{\Pi}_M \times_3 \boldsymbol{\Pi}_Q \tag{11}$$

where $\boldsymbol{\Pi}_n$ is an $n \times n$ exchange matrix having ones on its antidiagonal and zeros elsewhere. Exploiting the forward-backward averaging technique, the centro-Hermitian tensor [13] $\mathcal{Z}$ is formulated in the following fashion:

$$\mathcal{Z} = [\mathcal{X} \sqcup_3 \overline{\mathcal{X}}] \tag{12}$$

where $[\mathcal{A} \sqcup_n \mathcal{B}]$ denotes the concatenation of $\mathcal{A}$ and $\mathcal{B}$ along the nth mode. Owing to the special centro-Hermitian structure, $\mathcal{Z}$ can be transformed into a real-valued tensor by using unitary transformation which is given by

$$\overline{\mathcal{Z}} = \mathcal{Z} \times_1 \boldsymbol{U}_N^{\mathrm{H}} \times_2 \boldsymbol{U}_M^{\mathrm{H}} \times_3 \boldsymbol{U}_{2Q}^{\mathrm{H}} \tag{13}$$

where $\overline{\mathcal{Z}} \in \mathbb{R}^{N\times M\times 2Q}$ is a real-valued tensor and $\mathbf{U}$ is a unitary matrix defined as

$$\boldsymbol{U}_{2n} = \frac{1}{\sqrt{2}}\begin{bmatrix} \boldsymbol{I}_n & j\boldsymbol{I}_n \\ \boldsymbol{\Pi}_n & -j\boldsymbol{\Pi}_n \end{bmatrix} \tag{14}$$

if the subscript is even, or

$$\boldsymbol{U}_{2n+1} = \frac{1}{\sqrt{2}}\begin{bmatrix} \boldsymbol{I}_n & 0 & j\boldsymbol{I}_n \\ 0^{\mathrm{T}} & \sqrt{2} & 0^{\mathrm{T}} \\ \boldsymbol{\Pi}_n & 0 & -j\boldsymbol{\Pi}_n \end{bmatrix} \tag{15}$$

if the subscript is odd. From (12), the measurement data is doubled from Q to $2Q$. Increased estimation accuracy can, therefore, be achieved by replacing the measurement tensor $\mathcal{X} \in \mathbb{C}^{N\times M\times Q}$ by $\mathcal{Z} \in \mathbb{C}^{N\times M\times 2Q}$, which corresponds to forward-backward averaging of the data.

Now, using the properties introduced in Definition 4, we substitute (10) into (11) to obtain

$$\begin{aligned} \overline{\mathcal{X}} &= \mathcal{X}^* \times_1 \boldsymbol{\Pi}_N \times_2 \boldsymbol{\Pi}_M \times_3 \boldsymbol{\Pi}_Q \\ &= (\mathcal{I}_K \times_1 \boldsymbol{B}^* \times_2 \boldsymbol{A}^* \times_3 \boldsymbol{C}^* + \mathcal{N}^*) \times_1 \boldsymbol{\Pi}_N \times_2 \boldsymbol{\Pi}_M \times_3 \boldsymbol{\Pi}_Q \\ &= \mathcal{I}_K \times_1 \boldsymbol{\Pi}_N\boldsymbol{B}^* \times_2 \boldsymbol{\Pi}_M\boldsymbol{A}^* \times_3 \boldsymbol{\Pi}_Q\boldsymbol{C}^* + \overline{\mathcal{N}} \\ &= \mathcal{I}_K \times_1 \boldsymbol{B} \times_2 \boldsymbol{A} \times_3 \boldsymbol{\Pi}_Q\boldsymbol{C}^* + \overline{\mathcal{N}} \end{aligned} \tag{16}$$

where $\overline{\mathcal{N}} = \mathcal{N}^* \times_1 \boldsymbol{\Pi}_N \times_2 \boldsymbol{\Pi}_M \times_3 \boldsymbol{\Pi}_Q \in \mathbb{C}^{N\times M\times Q}$ denotes the noise tensor. In the derivation of (16), we use the fact that

$$\begin{aligned} \boldsymbol{\Pi}_M\boldsymbol{A}^* &= \boldsymbol{A} \\ \boldsymbol{\Pi}_N\boldsymbol{B}^* &= \boldsymbol{B} \end{aligned} \tag{17}$$

Then, substituting (16) into (12) we have

$$\begin{aligned} \mathcal{Z} &= [\mathcal{X} \sqcup_3 \overline{\mathcal{X}}] \\ &= [(\mathcal{I}_K \times_1 \boldsymbol{B} \times_2 \boldsymbol{A} \times_3 \boldsymbol{C} + \mathcal{N}) \sqcup_3 (\mathcal{I}_K \times_1 \boldsymbol{B} \times_2 \boldsymbol{A} \times_3 (\boldsymbol{\Pi}_Q\boldsymbol{C}^*) + \overline{\mathcal{N}})] \\ &= \mathcal{I}_K \times_1 \boldsymbol{B} \times_2 \boldsymbol{A} \times_3 \begin{bmatrix} \boldsymbol{C} \\ \boldsymbol{\Pi}_Q\boldsymbol{C}^* \end{bmatrix} + \widetilde{\mathcal{N}} \end{aligned} \tag{18}$$

where $\widetilde{\mathcal{N}} = [\mathcal{N} \sqcup_3 \overline{\mathcal{N}}] \in \mathbb{C}^{N\times M\times 2Q}$.

Next, inserting (18) into (13) yields

$$\begin{aligned} \overline{\mathcal{Z}} &= \mathcal{Z} \times_1 \boldsymbol{U}_N^{\mathrm{H}} \times_2 \boldsymbol{U}_M^{\mathrm{H}} \times_3 \boldsymbol{U}_{2Q}^{\mathrm{H}} \\ &= (\mathcal{I}_K \times_1 \boldsymbol{B} \times_2 \boldsymbol{A} \times_3 \begin{bmatrix} \boldsymbol{C} \\ \boldsymbol{\Pi}_Q\boldsymbol{C}^* \end{bmatrix} + \widetilde{\mathcal{N}}) \times_1 \boldsymbol{U}_N^{\mathrm{H}} \times_2 \boldsymbol{U}_M^{\mathrm{H}} \times_3 \boldsymbol{U}_{2Q}^{\mathrm{H}} \\ &= \mathcal{I}_K \times_1 \boldsymbol{U}_N^{\mathrm{H}}\boldsymbol{B} \times_2 \boldsymbol{U}_M^{\mathrm{H}}\boldsymbol{A} \times_3 \boldsymbol{U}_{2Q}^{\mathrm{H}} \begin{bmatrix} \boldsymbol{C} \\ \boldsymbol{\Pi}_Q\boldsymbol{C}^* \end{bmatrix} + \widehat{\mathcal{N}} \\ &= \mathcal{I}_K \times_1 \overline{\boldsymbol{B}} \times_2 \overline{\boldsymbol{A}} \times_3 \overline{\boldsymbol{C}} + \widehat{\mathcal{N}} \end{aligned} \tag{19}$$

where $\widehat{\mathcal{N}} = \widetilde{\mathcal{N}} \times_1 \boldsymbol{U}_N^{\mathrm{H}} \times_2 \boldsymbol{U}_M^{\mathrm{H}} \times_3 \boldsymbol{U}_{2Q}^{\mathrm{H}}$. According to Zoltowski et al. [16], matrices $\overline{\boldsymbol{A}} = \boldsymbol{U}_M^{\mathrm{H}}\boldsymbol{A}$ and $\overline{\boldsymbol{B}} = \boldsymbol{U}_N^{\mathrm{H}}\boldsymbol{B}$ are real-valued in (19).

Observing (19) and comparing it with (10), it is not difficult to find that when the noise term is ignored, the real-valued tensor $\overline{\mathcal{Z}}$ follows a PARAFAC model. Next, we try to calculate the real-valued loading matrices $\overline{\boldsymbol{A}} = \boldsymbol{U}_M^{\mathrm{H}}\boldsymbol{A}$ and $\overline{\boldsymbol{B}} = \boldsymbol{U}_N^{\mathrm{H}}\boldsymbol{B}$, in which the DOD and DOA information are included, respectively.

3.2. DOD and DOA estimation

In this part, we extract angle information from the real-valued loading matrices combined with traditional U-ESPRIT algorithm. However, different from [13,16,19], the proposed U-PARAFAC algorithm directly operates the real-valued loading factors instead of the real-valued signal subspace.

While the ALS method is attractive for its simplicity and satisfactory performance, it is not guaranteed to converge to a stationary point. Additionally, the ALS method becomes rather slow when targets are closely spaced, which indicates that the factors of the PARAFAC model are almost collinear (ill-conditioned cases). To solve these problems, the fast damped Gauss-Newton (dGN) algorithm [20] is introduced which requires less iterations than ALS while, for ill-conditioned cases, the performance is often superior.

Once the uniqueness of PARAFAC decomposition is guaranteed, the relationship between the estimated loading matrices $\boldsymbol{E}_{\mathbf{A}}$, $\boldsymbol{E}_{\mathbf{B}}$ and $\overline{\boldsymbol{A}}$, $\overline{\boldsymbol{B}}$ can be identified according to Definition 3. That is to say, there exists $K \times K$ real-valued matrices $\boldsymbol{\Lambda_1}$, $\boldsymbol{\Lambda_2}$ and $\boldsymbol{\Gamma}$ satisfying

$$\boldsymbol{E}_{\mathbf{A}} = \overline{\boldsymbol{A}}\boldsymbol{\Gamma}\boldsymbol{\Lambda}_{\mathbf{1}} \tag{20}$$

$$\boldsymbol{E}_{\mathbf{B}} = \overline{B}\boldsymbol{\Gamma}\boldsymbol{\Lambda}_{\mathbf{2}} \tag{21}$$

where $\boldsymbol{\Lambda_1}$, $\boldsymbol{\Lambda_2}$ and $\boldsymbol{\Gamma}$ are introduced in Definition 3. It is easy to find that $\boldsymbol{E}_{\mathbf{A}}$ and $\boldsymbol{E}_{\mathbf{B}}$ are obtained just by scaling and permuting the columns of $\overline{\boldsymbol{A}} = \boldsymbol{U}_M^{\mathrm{H}}\boldsymbol{A}$ and $\overline{\boldsymbol{B}} = \boldsymbol{U}_N^{\mathrm{H}}\boldsymbol{B}$, respectively. Note that the uniqueness property of PARAFAC implies that the kth column of both $\boldsymbol{E}_{\mathbf{A}}$ and $\boldsymbol{E}_{\mathbf{B}}$ contains the angle information of the kth target, which means that the DOD and DOA of the same target are automatically paired.

Different from Zoltowski et al. [16], U-ESPRIT algorithm is directly applied to operate the real-valued loading factors $\boldsymbol{E}_{\mathbf{A}}$ and $\boldsymbol{E}_{\mathbf{B}}$ instead of the real-valued signal subspace. Besides, additional angle pair-matching is not required anymore because the angle information of the targets can be extracted from the corresponding real-valued loading factors in PARAFAC model. Interestingly, we prove in Appendix B that the following equations are still satisfied:

$$\phi_{t,k}\boldsymbol{K}_{\mathbf{A},1}\boldsymbol{E}_{\mathbf{A}}(:,k) = \boldsymbol{K}_{\mathbf{A},2}\boldsymbol{E}_{\mathbf{A}}(:,k) \tag{22}$$

$$\phi_{r,k}\boldsymbol{K}_{\mathbf{B},1}\boldsymbol{E}_{\mathbf{B}}(:,k) = \boldsymbol{K}_{\mathbf{B},2}\boldsymbol{E}_{\boldsymbol{B}}(:,k) \tag{23}$$

where $\boldsymbol{E}_{\mathbf{A}}$ and $\boldsymbol{E}_{\mathbf{B}}$ are the real-valued loading factors instead of the real-valued signal subspace in [16]. $\phi_{t,\,k}$ and $\phi_{r,\,k}$ have the following forms:

$$\phi_{t,k} = \tan(\pi \sin\theta_k/2) \tag{24}$$

$$\phi_{r,k} = \tan(\pi \sin\varphi_k/2) \tag{25}$$

In (22) and (23), $\boldsymbol{K}_{\mathbf{A},1}$, $\boldsymbol{K}_{\mathbf{A},2}$, $\boldsymbol{K}_{\mathbf{B},1}$ and $\boldsymbol{K}_{\mathbf{B},2}$ are defined as

$$\begin{aligned}
\boldsymbol{K}_{\mathbf{A},1} &= \mathrm{Re}\left\{\boldsymbol{U}_{M-1}^{\mathrm{H}}\boldsymbol{J}_{t,2}\boldsymbol{U}_M\right\}\\
\boldsymbol{K}_{\mathbf{A},2} &= \mathrm{Im}\left\{\boldsymbol{U}_{M-1}^{\mathrm{H}}\boldsymbol{J}_{t,2}\boldsymbol{U}_M\right\}\\
\boldsymbol{K}_{\mathbf{B},1} &= \mathrm{Re}\left\{\boldsymbol{U}_{N-1}^{\mathrm{H}}\boldsymbol{J}_{r,2}\boldsymbol{U}_{\boldsymbol{N}}\right\}\\
\boldsymbol{K}_{\mathbf{B},2} &= \mathrm{Im}\left\{\boldsymbol{U}_{N-1}^{\mathrm{H}}\boldsymbol{J}_{t,2}\boldsymbol{U}_N\right\}
\end{aligned} \tag{26}$$

where $\boldsymbol{J}_{t,2} = [0, \boldsymbol{I}_{M-1}] \in \mathbb{R}^{(M-1)\times M}$ and $\boldsymbol{J}_{r,2} = [0, \boldsymbol{I}_{N-1}] \in \mathbb{R}^{(N-1)\times N}$ represent the selection matrices. Thus, $\phi_{t,\,k}$ and $\phi_{r,\,k}$ can be estimated by taking the least squares (LS) or total least squares (TLS) algorithm in (22) and (23). The solutions are given by

$$\phi_{t,k} = [\boldsymbol{K}_{\mathbf{A},1}\boldsymbol{E}_{\mathbf{A}}(:,k)]^{\dagger}[\boldsymbol{K}_{\mathbf{A},2}\boldsymbol{E}_{\mathbf{A}}(:,k)] \tag{27}$$

$$\phi_{r,k} = [\boldsymbol{K}_{\mathbf{B},1}\boldsymbol{E}_{\mathbf{B}}(:,k)]^{\dagger}[\boldsymbol{K}_{\mathbf{B},2}\boldsymbol{E}_{\mathbf{B}}(:,k)] \tag{28}$$

Then, the expressions of DOD and DOA can be derived as

$$\widehat{\theta}_k = \arcsin(2\arctan(\phi_{t,k})/\pi) \tag{29}$$

$$\widehat{\varphi}_k = \arcsin(2\arctan(\phi_{r,k})/\pi) \tag{30}$$

where $\widehat{\theta}_k$ and $\widehat{\varphi}_k$ are respectively the estimated DOD and DOA of the kth target.

3.3. Uniqueness and complexity analysis

In [18], the PARAFAC decomposition of the signal model $\mathcal{X}$ is referred to as the 2-D harmonic retrieval (HR) problem and some constraint conditions are proposed to guarantee the uniqueness of solutions, which actually determine the maximum number of targets that can be localized. However, the real-valued loading matrices $\overline{\boldsymbol{A}} = \boldsymbol{U}_M^{\mathrm{H}}\boldsymbol{A}$ and $\overline{\boldsymbol{B}} = \boldsymbol{U}_N^{\mathrm{H}}\boldsymbol{B}$ that we estimate in this paper is quite different, which really do not share the structure of Vandermonde matrix. Consequently, some constraint conditions presented in [18] may not be suitable in this paper.

Strictly speaking, uniqueness for the real-valued PARAFAC model is guaranteed if

$$k_{\overline{\mathbf{A}}} + k_{\overline{\mathbf{B}}} + k_{\overline{\mathbf{C}}} \geq 2K + 2 \tag{31}$$

which is first proved in [21]. $k_{\overline{\mathbf{A}}}$, $k_{\overline{\mathbf{B}}}$ and $k_{\overline{\mathbf{C}}}$ denote the Kruskal-rank [10] of the real-valued loading matrices $\overline{\boldsymbol{A}}$, $\overline{\boldsymbol{B}}$ and $\overline{\boldsymbol{C}}$. (31) determines the upper bound on the maximum number of targets that can be identified.

According to Phan et al. [20], the complexity of the proposed U-PARAFAC algorithm is $O(6MNQK + 27K^6)$ in each iteration, while the total number of iterations is much smaller compared with the traditional PARAFAC algorithm. The complexity of the PARAFAC algorithm is $O(3K^3 + 2(MN + MQ + NQ)K^2 + 6MNQK)$ for each iteration. Also, the solving process of the U-PARAFAC algorithm is real-valued, thus reducing the computation cost a lot for matrix inversion. For comparison, the computational cost of PM and U-ESPRIT algorithm are $O(MNQK + K^3)$ and $O(2M^2N^2Q + M^3N^3 + K^3)$, respectively. Hence, considering the number of iterations, the computational complexity of the U-PARAFAC algorithm is higher than other methods, but the performance shown later will prove the sacrifice is worthwhile.

4. Simulation results

Some simulations are conducted to demonstrate the improvement of the proposed U-PARAFAC algorithm in this section. The PM [7], the U-ESPRIT algorithm [8], the PARAFAC algorithm [11], the unitary tensor-ESPRIT algorithm [13], and the Cramer-Rao bound (CRB) for bistatic MIMO radar [22] are used to compare with the U-PARAFAC algorithm. In the first four simulations, the considered MIMO radar system is composed of $M = 4$ transmit antennas and $N = 6$ receive antennas. The mth transmitted waveform $\mathbf{s}_m$, i.e., the mth row of $\boldsymbol{S}$, is generated by $\boldsymbol{s_m} = (1 + \mathrm{j})/\sqrt{2}\boldsymbol{h}_m$, where $\boldsymbol{h}_m$ is the mth row of the $L \times L$ Hadamard matrix with $L = 256$. We assume that the additive noise is spatial and temporal white and the SNR is defined as

$$\mathrm{SNR} = 10\log_{10}\left(\sum_{q=1}^{Q} \| \boldsymbol{B}\boldsymbol{\Sigma}_q\boldsymbol{A}^{\mathrm{T}}\boldsymbol{S}\|_F^2 / \sum_{q=1}^{Q} \| \boldsymbol{W}_q\|_F^2\right)$$

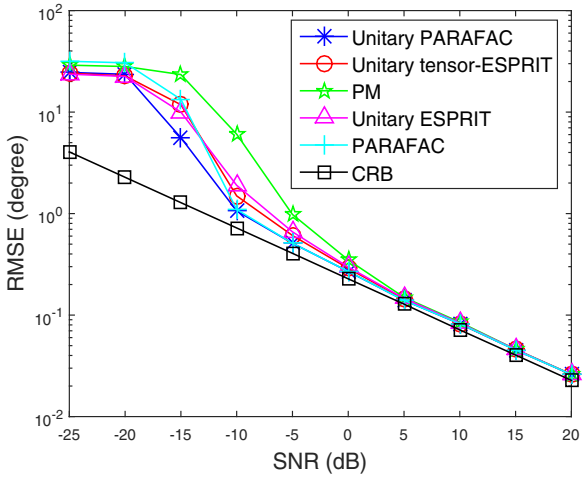

Fig. 1. RMSE versus SNR for $K = 2$ uncorrelated targets.

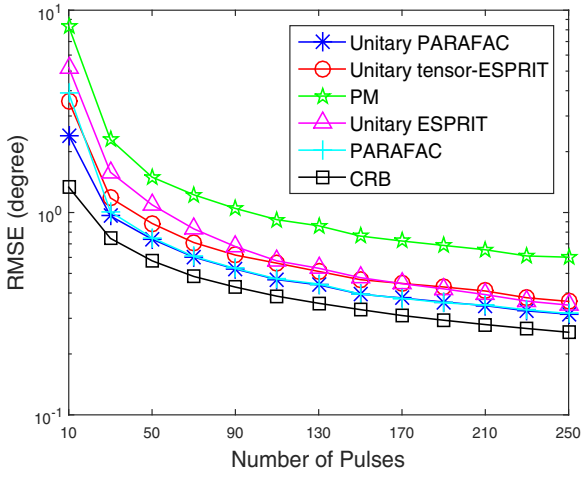

Fig. 2. RMSE versus the number of pulses for $K = 2$ uncorrelated targets.

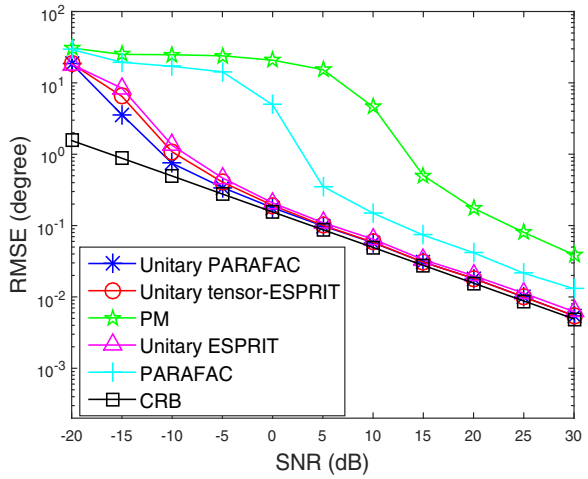

Fig. 3. RMSE versus SNR for $K = 2$ correlated targets.

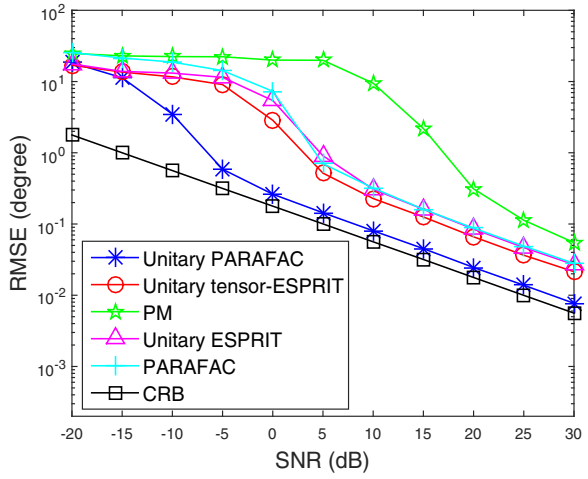

Fig. 4. RMSE versus SNR for $K = 3$ correlated targets.

All targets mentioned above follow the Swerling II model and the number of Monte Carlo trials P equals 200. We use the root mean square error (RMSE) to evaluate the performance of different algorithms, which is defined as

$$\mathrm{RMSE} = \sqrt{\frac{1}{2PK}\sum_{k=1}^{K}\sum_{p=1}^{P}[(\widehat{\theta}_{k,p}-\theta_k)^2 + (\widehat{\varphi}_{k,p}-\varphi_k)^2]}$$

where $\widehat{\theta}_{k,p}$ and $\widehat{\varphi}_{k,p}$ are respectively the estimated DOD and DOA for the kth target in the pth Monte Carlo trial.

In the first simulation, two uncorrelated targets located at $(\theta_1, \varphi_1) = (-40^\circ, -20^\circ)$ and $(\theta_2, \varphi_2) = (30^\circ, 20^\circ)$ are considered. Fig. 1 shows the RMSE versus SNR with $Q = 100$. As can been seen from Fig. 1, all the methods have the approximate performance at high SNR, but in low SNR region the U-PARAFAC algorithm has better performance than others, which implies that higher angle measurement accuracy can be obtained under the circumstances. Except the U-PARAFAC algorithm and the PARAFAC algorithm, all the above methods are generalized subspace-based approaches, which calculate the signal subspace by SVD, EVD or HOSVD and are sensitive to low SNR. Furthermore, compared with the traditional PARAFAC algorithm, the U-PARAFAC algorithm essentially doubles the number of pulses, which further guarantees a better performance. Fig. 2 shows the RMSE versus the number of pulses with SNR fixed at -5 dB and 400 independent simulations are carried out for each value of Q. It is indicated from Fig. 2 that the U-PARAFAC algorithm has better performance than other methods. Both Figs. 1 and 2 show the superiority of the proposed algorithm at low SNR.

When it comes to correlated targets, the U-ESPRIT algorithm, the unitary tensor-ESPRIT algorithm and the method in [19] all adopt the forward-backward averaging and can separate two completely coherent targets. Since the method in [19] takes the mutual coupling into consideration, we do not take it for comparison here. In the second simulation, two highly correlated targets are located at $(\theta_1, \varphi_1) = (-40^\circ, -30^\circ)$ and $(\theta_2, \varphi_2) = (0^\circ, 10^\circ)$, respectively. The correlation coefficient between the two targets is 0.99 and the number of pulses is 200. As shown in Fig. 3, the U-PARAFAC algorithm, the U-ESPRIT algorithm and the unitary tensor-ESPRIT algorithm show the good performance in dealing with no more than two correlated targets because of the application of forward-backward averaging. The U-PARAFAC algorithm still has better performance in low SNR.

The third simulation is conducted to evaluate the performance when the number of correlated targets is more than two. In this case, we consider $K = 3$ correlated targets, which are located at $(\theta_1, \varphi_1) = (-40^\circ, -20^\circ)$, $(\theta_2, \varphi_2) = (25^\circ, 0^\circ)$ and $(\theta_3, \varphi_3) = (40^\circ, 20^\circ)$, respectively. The correlation coefficients between the first two targets, as well as the first and third targets are both 0.99. The performance curves versus SNR are drawn in Fig. 4 with the number of pulses Q fixed at 200. It is shown that the performance of the U-ESPRIT algorithm and the unitary tensor-

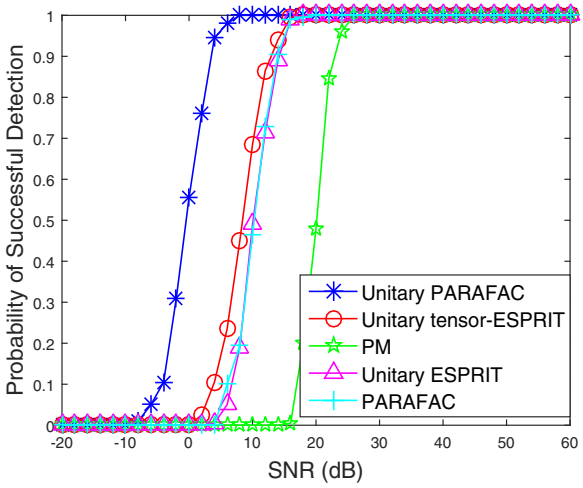

Fig. 5. Probability of successful detection versus SNR for $K = 3$ correlated targets.

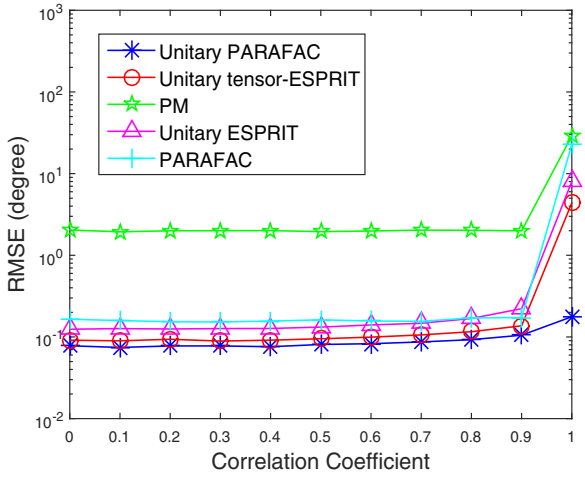

Fig. 6. RMSE versus the correlation coefficient for $K = 3$ targets.

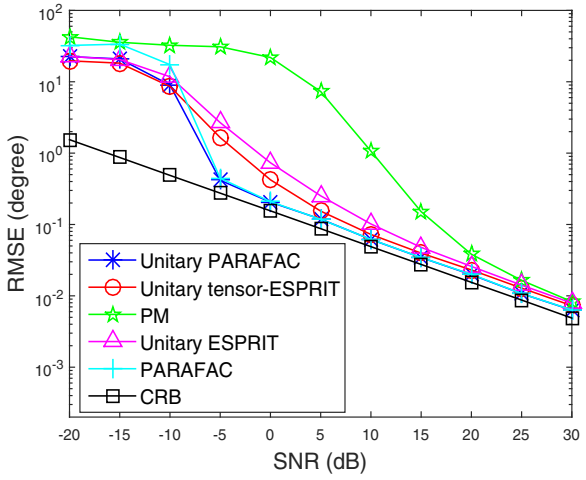

Fig. 7. RMSE versus SNR for $K = 2$ closely spaced targets.

ESPRIT algorithm degrades greatly, because the number of correlated targets is more than two. Conversely, the U-PARAFAC algorithm still performs well even without sacrificing any array aperture because of the forward-backward averaging operation and the avoidance of calculating the signal subspace. It is well known that subspace-based algorithms perform poorly when highly correlated or coherent sources are present [23]. Taking the PARAFAC model means avoiding calculating the signal subspace.

In the simulation conditions given above, Fig. 5 shows the probability of successful detection versus SNR. All targets can be seen as successful detection when the absolute errors of DOD and DOA for all targets are within 0.5°. The results indicate that, although all the methods exhibit a 100% successful detection in high SNR region, the probability of successful detection of all methods starts dropping at a certain point with the decrease of SNR, called SNR threshold. The proposed algorithm has the lowest SNR threshold compared with other methods. Both Figs. 4 and 5 show the good performance of the proposed algorithm in dealing with more than two correlated targets, which is a direct result of the combination of the PARAFAC model and the forward-backward averaging technique.

In the fourth simulation, the decorrelation ability of all methods is tested with the SNR fixed at 10dB. In this example, three targets are located at $(\theta_1, \varphi_1) = (-20^\circ, -30^\circ)$, $(\theta_2, \varphi_2) = (10^\circ, 20^\circ)$ and $(\theta_3, \varphi_3) = (50^\circ, 60^\circ)$ and the number of pulses $Q = 200$. The correlation coefficient between the first two targets is fixed at 0.99, while between the first and third targets the correlation coefficient is varied from 0 to 1 gradually. As demonstrated in Fig. 6, the RMSE of the proposed algorithm remains relatively stable, while the performance of other methods seriously degrades when the correlation coefficient approaches to one. This indicates that the U-PARAFAC algorithm has the superiority in addressing more than two highly correlated targets.

In the fifth simulation, we test the performance for closely spaced targets. Two closely spaced targets are located at $(\theta_1, \varphi_1) = (40^\circ, 10^\circ)$ and $(\theta_2, \varphi_2) = (43^\circ, 13^\circ)$, respectively. The number of pulses is $Q = 100$. With $M = 8$ transmit and $N = 10$ receive antennas, all targets are uncorrelated with each other. In fact, closely spaced targets mean ill-conditioned steering matrices (or signal subspace), which makes the separation more difficult for subspace-based methods. The proposed U-PARAFAC algorithm does not require to estimate the signal subspace and exploits the technique of forward-backward averaging, which results in superior performance. As shown in Fig. 7, the U-PARAFAC algorithm and the PARAFAC algorithm perform better than other subspace-based methods in high SNR region by taking a PARAFAC model, while the U-PARAFAC algorithm performs better in low SNR region.

5. Conclusion

In this paper, a novel unitary PARAFAC algorithm is proposed for angle estimation in bistatic MIMO radar. A real-valued tensor model is constructed by using the traditional forward-backward averaging technique. Significantly, we prove this real-valued model is a PARAFAC model. Hence, this real-valued tensor model can be decomposed through PARAFAC method instead of using the HOSVD technique, which does not require to estimate the signal subspace. Moreover, the U-ESPRIT method is firstly extended to the real-valued PARAFAC model, which directly operates the real-valued loading factors instead of the signal subspace. Without sacrificing array aperture, the proposed U-PARAFAC algorithm shows excellent performance especially when dealing with $K > 2$ highly correlated targets. The proposed algorithm also provides a light performance improvement at low SNR. Additional angle pair-matching is not required. Simulation results demonstrate the effectiveness of the proposed algorithm.

Acknowledgments

The authors wish to thank the anonymous reviewers for their valuable suggestions on improving this paper. This research did

not receive any specific grant from funding agencies in the public, commercial, or not-for-profit sectors.

Appendix A

To verify the equivalence of (9) and (10), we need only to identify that each frontal slice [10] of the third-order tensor $\mathcal{X} = \mathcal{I}_K \times_1 \boldsymbol{B} \times_2 \boldsymbol{A} \times_3 \boldsymbol{C}$ owns the same structure with (8). Without considering the effect of noise, the qth frontal slice of $\mathcal{X} = \mathcal{I}_K \times_1 \boldsymbol{B} \times_2 \boldsymbol{A} \times_3 \boldsymbol{C}$ is denoted by

$$\boldsymbol{\Psi}_q = \mathcal{I}_K \times_1 \boldsymbol{B} \times_2 \boldsymbol{A} \times_3 \boldsymbol{c}_q^{\mathrm{T}} \tag{A.1}$$

where $\boldsymbol{c}_q^{\mathrm{T}} \in \mathbb{C}^{1\times K}$ is the qth row of the matrix $\boldsymbol{C}$. $\boldsymbol{\Psi}_q$ is an $N \times M$ matrix. Actually, $\boldsymbol{\Psi}_q$ is also a special third-order tensor whose third dimension length is one. Then, according to Koida and Bader [10], the mode-1 matricization of $\boldsymbol{\Psi}_q$ is unchanged. We have

$$\boldsymbol{\Psi}_q = \boldsymbol{B}\boldsymbol{I}_{K,(1)}\left(\boldsymbol{c}_q^{\mathrm{T}} \otimes \boldsymbol{A}\right)^{\mathrm{T}} \tag{A.2}$$

where $\boldsymbol{I}_{K,(1)} \in \mathbb{R}^{K\times K^2}$ denotes the mode-1 matricization of identity tensor $\mathcal{I}_K$. There exists

$$\boldsymbol{I}_{K,(1)} = [\boldsymbol{\Omega}_1,\ \boldsymbol{\Omega}_2, \ldots,\ \boldsymbol{\Omega}_K] \tag{A.3}$$

where $\boldsymbol{\Omega}_k$ is a $K \times K$ matrix in which the kth element of main diagonal is one and other elements are zero. Next, we have

$$\boldsymbol{I}_{K,(1)}\left(\boldsymbol{c}_q^{\mathrm{T}} \otimes \boldsymbol{A}\right)^{\mathrm{T}} = \left[\boldsymbol{c}_{q,1}\boldsymbol{a}_1,\ \boldsymbol{c}_{q,2}\boldsymbol{a}_2, \ldots, \boldsymbol{c}_{q,K}\boldsymbol{a}_K\right]^{\mathrm{T}} \tag{A.4}$$

where $\boldsymbol{c}_{q,k}$ is the kth element of the vector $\boldsymbol{c}_q$. Finally, inserting (A.4) into (A.2) yields

$$\begin{aligned}\boldsymbol{\Psi}_q &= \boldsymbol{B}\left[\boldsymbol{c}_{q,1}\boldsymbol{a}_1,\ \boldsymbol{c}_{q,2}\boldsymbol{a}_2, \ldots, \boldsymbol{c}_{q,K}\boldsymbol{a}_K\right]^{\mathrm{T}} \\ &= \boldsymbol{B}\boldsymbol{\Sigma}_q\boldsymbol{A}^{\mathrm{T}}\end{aligned} \tag{A.5}$$

Comparing (A.5) with (8), we can find that $\boldsymbol{\Psi}_q$ shares the same structure with $\boldsymbol{Y}_q$ without considering the effect of noise. Consequently, the equivalence of (9) and (10) is guaranteed.

Appendix B

According to (20) and (21), we have

$$\boldsymbol{E}_{\mathbf{A}}(:,k) = \boldsymbol{U}_M^{\mathrm{H}}\boldsymbol{A}\boldsymbol{\Gamma}\boldsymbol{\Lambda}_1(:,k) = \lambda_k\boldsymbol{U}_M^{\mathrm{H}}\widehat{\boldsymbol{A}}(:,k) \tag{B.1}$$

$$\boldsymbol{E}_{\mathbf{B}}(:,k) = \boldsymbol{U}_N^{\mathrm{H}}\boldsymbol{B}\boldsymbol{\Gamma}\boldsymbol{\Lambda}_2(:,k) = \boldsymbol{\gamma}_k\boldsymbol{U}_N^{\mathrm{H}}\widehat{\boldsymbol{B}}(:,k) \tag{B.2}$$

where $\widehat{\boldsymbol{A}} = \boldsymbol{A}\boldsymbol{\Gamma}$ and $\widehat{\boldsymbol{B}} = \boldsymbol{B}\boldsymbol{\Gamma}$, while λ_k and γ_k are the kth diagonal element of $\boldsymbol{\Lambda}_1$ and $\boldsymbol{\Lambda}_2$, respectively.

Thus, the LS solutions of (22) and (23) are given by

$$\begin{aligned}\phi_{\mathrm{t},k} &= [\boldsymbol{K}_{\mathbf{A},1}\boldsymbol{E}_{\mathbf{A}}(:,k)]^{\dagger}[\boldsymbol{K}_{\mathbf{A},2}\boldsymbol{E}_{\mathbf{A}}(:,k)] \\ &= \left[\lambda_k\boldsymbol{K}_{\mathbf{A},1}\boldsymbol{U}_M^{\mathrm{H}}\widehat{\boldsymbol{A}}(:,k)\right]^{\dagger}\left[\lambda_k\boldsymbol{K}_{\mathbf{A},2}\boldsymbol{U}_M^{\mathrm{H}}\widehat{\boldsymbol{A}}(:,k)\right] \\ &= \left[\boldsymbol{K}_{\mathbf{A},1}\boldsymbol{U}_M^{\mathrm{H}}\widehat{\boldsymbol{A}}(:,k)\right]^{\dagger}\left[\boldsymbol{K}_{\mathbf{A},2}\boldsymbol{U}_M^{\mathrm{H}}\widehat{\boldsymbol{A}}(:,k)\right]\end{aligned} \tag{B.3}$$

$$\begin{aligned}\phi_{\mathrm{r},k} &= [\boldsymbol{K}_{\mathbf{B},1}\boldsymbol{E}_{\mathbf{B}}(:,k)]^{\dagger}[\boldsymbol{K}_{\mathbf{B},2}\boldsymbol{E}_{\mathbf{B}}(:,k)] \\ &= \left[\gamma_k\boldsymbol{K}_{\mathbf{B},1}\boldsymbol{U}_N^{\mathrm{H}}\widehat{\boldsymbol{B}}(:,k)\right]^{\dagger}\left[\gamma_k\boldsymbol{K}_{\mathbf{B},2}\boldsymbol{U}_N^{\mathrm{H}}\widehat{\boldsymbol{B}}(:,k)\right] \\ &= \left[\boldsymbol{K}_{\mathbf{B},1}\boldsymbol{U}_N^{\mathrm{H}}\widehat{\boldsymbol{B}}(:,k)\right]^{\dagger}\left[\boldsymbol{K}_{\mathbf{B},2}\boldsymbol{U}_N^{\mathrm{H}}\widehat{\boldsymbol{B}}(:,k)\right]\end{aligned} \tag{B.4}$$

Since matrices $\widehat{\boldsymbol{A}}$ and $\widehat{\boldsymbol{B}}$ are the results of exchanging the columns of $\boldsymbol{A}$ and $\boldsymbol{B}$ in the same order, the columns of $\widehat{\boldsymbol{A}}$ and $\widehat{\boldsymbol{B}}$ are still conjugate centrosymmetric. Then, the conclusion in [16] is exploited, which is shown as

$$\tan(\pi\sin\theta_k/2)\boldsymbol{K}_{\mathbf{A},1}\boldsymbol{U}_M^{\mathrm{H}}\widehat{\boldsymbol{A}}(:,k) = \boldsymbol{K}_{\mathbf{A},2}\boldsymbol{U}_M^{\mathrm{H}}\widehat{\boldsymbol{A}}(:,k) \tag{B.5}$$

$$\tan(\pi\sin\varphi_k/2)\boldsymbol{K}_{\mathbf{B},1}\boldsymbol{U}_N^{\mathrm{H}}\widehat{\boldsymbol{B}}(:,k) = \boldsymbol{K}_{\mathbf{B},2}\boldsymbol{U}_N^{\mathrm{H}}\widehat{\boldsymbol{B}}(:,k) \tag{B.6}$$

where $\boldsymbol{U}_M^{\mathrm{H}}\widehat{A}(:,k)$ and $\boldsymbol{U}_N^{\mathrm{H}}\widehat{B}(:,k)$ share the same structure of $\boldsymbol{d}_N(\mu)$ in [16]. Combining (B.3), (B.4), (B.5), and (B.6) together, it is not difficult to find that

$$\phi_{\mathrm{t},k} = \tan(\pi\sin\theta_k/2) \tag{B.7}$$

$$\phi_{r,k} = \tan(\pi\sin\varphi_k/2) \tag{B.8}$$

Supplementary material

Supplementary material associated with this article can be found, in the online version, at 10.1016/j.combustflame.2015.09.001

References

[1] E. Fisher, A. Haimovich, R. Blum, Spatial diversity in radars-models and detection performance, IEEE Trans. Signal Process 54 (3) (2006) 823–838.
[2] L. Xu, J. Li, P. Stoica, Target detection and parameter estimation for MIMO radar system, IEEE Trans. Aerosp. Electron. Syst 44 (3) (2008) 927–939.
[3] A.M. Haimovich, R. Blum, L. Cimini, MIMO radar with widely separated antennas, IEEE Signal Process. Mag 25 (1) (2008) 116–129.
[4] J. Li, P. Stoica, MIMO radar with colocated antennas, IEEE Signal Process. Mag 24 (5) (2007) 106–114.
[5] H. Yan, J. Li, G. Liao, Multitarget identification and localization using bistatic MIMO radar systems, EURASIP J. Adv. Signal Process (2008) 1–8.
[6] C. Duofang, C. Baixiao, Q. Guodong, Angle estimation using ESPRIT in MIMO radar, Electron. Lett 44 (12) (2008) 770–771.
[7] Z.D. Zheng, J.Y. Zhang, Fast method for multi-target localization in bistatic MIMO radar, Electron. Lett 47 (2) (2011) 138–139.
[8] G. Zheng, B. Chen, M. Yang, Unitary ESPRIT algorithm for bistatic MIMO radar, Electron. Lett 48 (3) (2012) 179–181.
[9] M. Haardt, J.A. Nossek, Unitary ESPRIT: how to obtain increased estimation accuracy with a reduced computational burden, IEEE Trans. Signal Process 43 (5) (1995) 1232–1242.
[10] T.G. Kolda, B.W. Bader, Tensor decomposition and application, SIAM Rev 51 (3) (2009) 455–500.
[11] D. Nion, N.D. Sidiropoulos, A PARAFAC-based technique for detection and localization of multiple targets in a MIMO radar system, in Proc. IEEE Int. Conf. Acoust., Speech, Signal Process. Taipei, Taiwan, April (2009) 2077–2080.
[12] Y. Cheng, R. Yu, H. Gu, W. Su, Multi-SVD based subspace estimation to improve angle estimation accuracy in bistatic MIMO radar, Signal Process. 93 (7) (2013) 2003–2009.
[13] M. Haardt, F. Roemer, G.D. Galdo, Higher-order SVD-based subspace estimation to improve the parameter estimation accuracy in multidimensional harmonic retrieval problems, IEEE Trans. Signal Process. 56 (7) (2008) 3198–3213.
[14] T.J. Shan, M. Wax, T. Kailath, On spatial smoothing for direction of arrival estimation of coherent signals, IEEE Trans. Acoust. Speech Signal Process. 33 (4) (1985) 806–811.
[15] N.D. Sidiropoulos, R. Bro, G.B. Giannakis, Parallel factor analysis in sensor array processing, IEEE Trans. Signal Process. 48 (8) (2000) 2377–2388.
[16] M.D. Zoltowski, M. Haardt, C.P. Mathews, Closed-form 2-d angle estimation with rectangular arrays in element space or beamspace via unitary ESPRIT, IEEE Trans. Signal Process. 44 (2) (1996) 316–328.
[17] L.T. Huang, A.L.F. de Almeida, H.C. So, Target estimation in bistatic MIMO radar via tensor completion, Signal Process. 120 (2016) 654–659.
[18] D. Nion, N.D. Sidiropoulos, Tensor algebra and multidimensional harmonic retrieval in signal processing for MIMO radar, IEEE Trans. Signal Process. 58 (11) (2010) 5693–5705.
[19] X. Wang, W. Wang, J. Liu, Q. Liu, B. Wang, Tensor-based real-valued subspace approach for angle estimation in bistatic MIMO radar with unknown mutual coupling, Signal Process. 116 (2015) 152–158.
[20] A.H. Phan, P. Tichavsky, A. Cichocki, Low complexity damped gauss-newton algorithms for CANDECOMP/PARAFAC, SIAM J. Matrix Anal. Appl. 34 (1) (2013) 126–147.
[21] J.B. Kruskal, Three way arrays: rank and uniqueness of trilinear decompositions with applications to arithmetic complexity and statistics, Linear Algebra Appl. 18 (2) (1977) 95–138.
[22] X. Zhang, Z. Xu, L. Xu, D. Xu, Trilinear decomposition-based transmit angle and receive angle estimation for multiple-input multiple-output radar, IET Radar Sonar Navig. 5 (6) (2011) 626–631.
[23] R.T. Williams, S. Prasad, A.K. Mahalanabis, L.H. Sibul, An improved spatial smoothing technique for bearing estimation in a multipath environment, IEEE Trans. Acoust. Speech Signal Process. 36 (4) (1988) 425–432.